Arbitrarily high-order globally divergence-free DG method for compressible ideal MHD equations on unstructured meshes

Yuchang Liu[1], Yan Jiang[2 3], and Mengping Zhang[4]

Abstract: A simple, general framework is proposed to construct arbitrary order globally divergence-free discontinuous Galerkin (DG) scheme for ideal magnetohydrodynamic (MHD) equations on unstructured meshes. Similar to the approaches in [3, 41], our framework defines normal magnetic components on edges, updates them over time, and then uses these to reconstruct the globally divergence-free magnetic field. In particular, we design the 1D updating scheme for the normal magnetic component on each edge, and enhance the numerical flux selection to improve stability. Additionally, we achieve a significant improvement by utilizing mesh geometry and introducing variable substitution, resulting in a cell-independent reconstruction formulation that is both efficient and easy to implement. Numerical experiments confirm both the efficiency and effectiveness of our proposed method.

Key Words: discontinuous Galerkin method, high-order accuracy, magnetohydrodynamics, globally divergence-free, unstructured meshes.

1 Introduction

In this study, we investigate the compressible ideal magnetohydrodynamic (MHD) equations, which describe the motion of charged fluids or charged particles such as plasmas, electrolytes, and liquid metals. MHD equations are widely applied in space weather forecasting, astrophysics, plasma physics, and engineering. Recent advances in high-order methods have enabled researchers to achieve high-resolution solutions with reduced computational cost, such as finite difference methods [10, 31], finite volume methods [3], spectral methods [30], finite element methods [21], and discontinuous Galerkin (DG) methods [24, 29, 5]. This study specifically focuses on the DG method.

The DG method was first proposed by Reed and Hill in 1973 [34] for solving neutron transport equations. Cockburn and Shu made significant improvements to it, proposing

---

[1] School of Mathematical Sciences, University of Science and Technology of China, Hefei, Anhui 230026, P.R. China. E-mail: lissandra@mail.ustc.edu.cn.

[2] School of Mathematical Sciences, University of Science and Technology of China, Hefei, Anhui 230026, P.R. China. E-mail: jiangy@ustc.edu.cn. Research supported by NSFC grant 12271499.

[3] Laoshan Laboratory, Qingdao 266237, China.

[4] School of Mathematical Sciences, University of Science and Technology of China, Hefei, Anhui 230026, P.R. China. E-mail: mpzhang@ustc.edu.cn.

the Runge-Kutta DG (RKDG) framework [14, 13, 11, 15, 16] for hyperbolic conservation laws. This framework uses DG discretization in space, strong stability-preserving Runge-Kutta (SSP-RK) methods in time, and applies nonlinear limiters at each RK stage to suppress numerical oscillations near discontinuities. The DG method offers several advantages, including flexibility, conservation properties, support for hanging nodes, and high parallel efficiency.

Mathematically, the MHD equation is a set of nonlinear conservation laws governing mass, momentum, energy, and magnetic field. Additionally, the magnetic field must satisfy a crucial divergence-free constraint. That is, if the initial magnetic field has zero divergence, then the exact solution maintains zero magnetic field divergence at any time. A major challenge in numerical simulation of MHD equations is preserving the divergence-free property in the discrete sense. In fact, most of the standard numerical methods can not directly satisfy this condition, leading to computational instability [4]. To overcome this challenge, researchers have developed four primary approaches in the literature: 8-wave formulation [33], projection methods [37], divergence cleaning methods [17, 8], and constrained transport methods [18, 1, 10, 43].

In particular, the DG methods are primarily incorporated within the constrained transport framework. In [12], Cockburn, Li, and Shu first proposed the locally divergence-free method for Maxwell equations, then Li and Shu extended it to MHD equations [24]. This method employs a specialized finite element space for the magnetic field, ensuring the divergence of magnetic field is exactly zero inside each cell. However, the magnetic field remains discontinuous across cell interfaces, resulting in the failure of divergence-free condition globally. To address this, inspired by the finite volume method in [2], Li et al. proposed the globally divergence-free central DG framework in [26, 25]. These methods define normal magnetic components as univariate polynomials on cell interfaces, update them using the magnetic induction equation, and subsequently reconstruct a globally divergence-free interior magnetic field at each RK stage using these components. This approach has been extensively developed and applied within the DG framework [19, 7, 5, 27, 28].

However, the aforementioned work has all been conducted on structured meshes. For unstructured meshes, the situation becomes more complex. When defining the normal magnetic components, the geometric information of the mesh must also be considered, and the updating scheme for the normal magnetic components needs to be carefully redesigned. Moreover, reconstructing the magnetic field on unstructured meshes becomes more difficult. In [41], a finite volume weighted essentially non-oscillatory (WENO) method was proposed, which first designs the updating scheme for induction equations on unstructured meshes. This work only realized third-order accuracy since the complexity of their reconstruction. Moreover, the numerical flux design in this work employs a simplistic approach, failing to simultaneously account for contributions from both horizontal and vertical directions. This work has been extended to central DG methods and central finite volume methods in [42]. The reconstruction is also complex, and they only realized second-order accuracy. To simplify the reconstruction, Balsara et al. proposed the least-squares reconstruction in finite volume framework [3], which provides a unified framework for arbitrary order accuracy and successfully achieved reconstructions up to fifth order. However, this reconstruction depends on the geometry of cell. Therefore, either it requires solving a linear system on each cell, or it demands substantial memory to store pre-computed inverse matrices for every cell.

In this work, we are aiming to construct a globally divergence-free DG scheme for unstructured meshes under this framework, which addresses the aforementioned challenges. Based on the foregoing discussions, there are two key points in the design of the scheme. The first is the updating scheme of induction equation for the normal magnetic components on edges. In this regard, we carefully redesign the 1D and 2D numerical fluxes to construct the updating scheme, which is an improvement of the selection in [41]. The second is the reconstruction in cells. In this regard, we follow the idea of Balsara in [3], but by utilizing the geometry of mesh, we introduce a cell-independent least-squares reconstruction with a variable substitution, which can significantly enhance efficiency while maintaining the accuracy. In principle, it is also applicable to moving meshes. To the best of our knowledge, this is the first globally divergence-free DG method for unstructured meshes. Moreover, similar to [3], our framework also provides a unified approach for any order of finite element space, but offers simpler implementation.

The rest of this paper is organized as follows. Section 2 presents a detailed formulation of the globally divergence-free DG scheme and its implementation. In Section 3, various numerical examples are provided to demonstrate the efficiency and effectiveness of the proposed scheme. Section 4 concludes with a discussion of the findings.

2 Numerical method

We consider the two-dimensional ideal MHD equations

$$\frac{\partial \mathbf{q}}{\partial t} + \nabla \cdot \mathbf{F}(\mathbf{q}) = \mathbf{0}, \tag{2.1}$$

where $\mathbf{q} = (\rho, u_x, u_y, u_z, \mathcal{E}, B_x, B_y, B_z)^T$,

$$\mathbf{F}(\mathbf{q}) = \begin{bmatrix} \rho u_x & \rho u_y \\ \rho u_x^2 + p^\star - B_x^2 & \rho u_x u_y - B_x B_y \\ \rho u_x u_y - B_x B_y & \rho u_y^2 + p^\star - B_y^2 \\ \rho u_x u_z - B_x B_z & \rho u_y u_z - B_y B_z \\ u_x(\mathcal{E} + p^\star) - B_x(\mathbf{u}\cdot\mathbf{B}) & u_y(\mathcal{E} + p^\star) - B_y(\mathbf{u}\cdot\mathbf{B}) \\ 0 & u_y B_x - u_x B_y \\ u_x B_y - u_y B_x & 0 \\ u_x B_z - u_z B_x & u_y B_z - u_z B_y \end{bmatrix},$$

with

$$\mathcal{E} = \frac{p}{\gamma - 1} + \frac{1}{2}\rho \left\|\mathbf{u}\right\|^2 + \frac{1}{2}\left\|\mathbf{B}\right\|^2. \tag{2.2}$$

Here, ρ is the mass density, $\rho\mathbf{u}$ is the momentum, $\mathcal{E}$ is the total energy, p is the hydrodynamic pressure, $\mathbf{B}$ is the magnetic field, $\gamma = 5/3$ is the ideal gas constant, $p^\star = p + \left\|\mathbf{B}\right\|^2/2$ is the total pressure, and $\|\cdot\|$ denotes the Euclidean vector norm. Taking divergence of the magnetic field equation yields

$$\frac{\partial\left(\nabla\cdot\mathbf{B}\right)}{\partial t} = 0.$$

Hence, if the divergence of the exact magnetic field is zero initially, then it will remain zero for all time, i.e.

$$\nabla\cdot\mathbf{B} = 0. \tag{2.3}$$

This is called the *divergence-free* property. A main challenge for numerical schemes is to preserve this property in a discrete sense. Otherwise, the failure in preserving this property may cause non-physical structure and numerical instabilities in the simulation. In this work, we are aiming to design a high-order DG method for the MHD equation (2.1) on unstructured meshes, which maintains the divergence-free property globally.

2.1 Runge-Kutta discontinuous Galerkin framework

Assume the computational domain Ω is covered by shape-regular non-overlapping triangles $\mathcal{K} = \{K\}$ with edges $\mathscr{E} = \{e : e \subset \partial K\}$. The maximum and minimum lengths of the edges in the mesh are denoted by h_{max} and h_{min}. Without loss of generality, we number the vertices $P_1,\ P_2,\ P_3$ of a cell in anticlockwise order. In particular, we assume e_i is the opposite edge of P_i. And the unit outer normal vectors on e_i is denoted by $\mathbf{n}_i$. A schematic diagram is shown in Fig. 2.1.

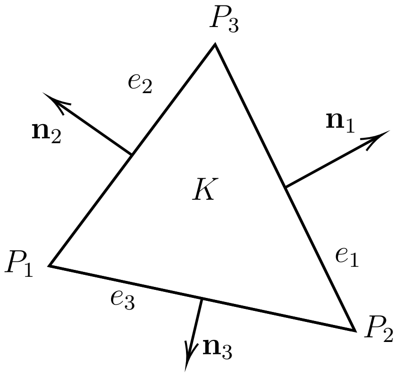

Figure 2.1. The notations of a cell K.

Define the finite element space

$$V_h^k = \left\{ w(x,y): \ w(x,y)|_K \in \mathbb{P}^k(K), \ \forall K \in \mathcal{K} \right\}. \tag{2.4}$$

Then, the vector finite element space is defined as $\mathbf{V}_h^k = [V_h^k]^8$. The semi-discrete DG scheme reads: Find $\mathbf{q}_h \in \mathbf{V}_h^k$, such that for any $K \in \mathcal{K}$ and $\mathbf{w} \in \mathbf{V}_h^k$,

$$\int_K \frac{\partial \mathbf{q}_h}{\partial t} \cdot \mathbf{w} \mathrm{d}K - \int_K \mathbf{F}\left(\mathbf{q}_h\right) : \nabla \mathbf{w} \mathrm{d}K + \sum_{e \subset \partial K} \int_e \mathbf{h}\left(\mathbf{q}^{int}, \mathbf{q}^{ext}, \mathbf{n}\right) \cdot \mathbf{w} \mathrm{d}s = 0. \tag{2.5}$$

Here, $\mathbf{q}^{int}$, $\mathbf{q}^{ext}$ are one-sided limiters from inside and outside of the cell K respectively, $\mathbf{n}$ is the unit outer normal vector of edge e, and $\mathbf{h}$ is the numerical flux consistent with $\mathbf{F}(\mathbf{q}) \cdot \mathbf{n}$. In this paper, the Lax-Friedrichs (LF) flux is considered

$$\mathbf{h}(\mathbf{q}^-, \mathbf{q}^+, \mathbf{n}) = \frac{1}{2}\left(\mathbf{F}(\mathbf{q}^-) + \mathbf{F}(\mathbf{q}^+)\right) \cdot \mathbf{n} - \frac{1}{2}\alpha(\mathbf{q}^+ - \mathbf{q}^-), \tag{2.6}$$

where α is the local maximal absolute wave speed along direction $\mathbf{n}$. It is computed in the same way as in [10].

The semi-discrete DG discretization (2.5) can be treated as an ODE system

$$\frac{\mathrm{d}\mathbf{q}_h}{\mathrm{d}t} = \mathcal{L}_h(\mathbf{q}_h).$$

In this work, it is evolved by the 10-stage, fourth-order Runge-Kutta method by Ketcheson [22]. Since it is a combination of Euler forward, we will take Euler forward as an example in the following discussion. All algorithms and theoretical analysis can be extended to Runge-Kutta directly.

2.2 The globally divergence-free method

It is known that the scheme (2.5) does not necessarily satisfy the divergence-free condition. In this subsection, following the framework in [25, 19, 5], we will construct the globally divergence-free (GDF) DG method on unstructured meshes.

First, we recall the definition of a GDF vector field:

Definition 2.1 (Globally divergence-free)**.** *A piecewise smooth vector field $\mathbf{B}_h$ on mesh $\mathcal{K}$ is called **globally divergence-free**, if*

1. *The interior divergence $\nabla \cdot \mathbf{B}_h = 0$ in each cell $K \in \mathcal{K}$,*
2. *The normal component $\mathbf{B}_h \cdot \mathbf{n}$ is continuous at each edge $e \in \mathscr{E}$.*

In [12, 24], a special locally divergence-free (LDF) finite element space is defined for the magnetic field $\mathbf{B}$, which satisfies the first condition. However, in their schemes, the normal magnetic component still has jumps across the edges, hence fails in preserving the GDF property. To satisfy the second condition, we can define the normal magnetic component on each edge e as a univariate polynomial, update it in time, and then use them to reconstruct a GDF interior magnetic field.

In particular, consider an edge e. Denote its unit normal direction as $\mathbf{n} = (n_1, n_2)^T$, and its unit direction as $\mathbf{m} = (m_1, m_2)^T$, satisfying $(m_1, m_2) = (-n_2, n_1)$. The starting point and ending point of e along $\mathbf{m}$-direction are denoted by $P_{start} = (x_{start}, y_{start})$ and $P_{end} = (x_{end}, y_{end})$ respectively. Note that the normal component $\mathbf{B}\cdot\mathbf{n}$ is a scalar function along this edge, we can define a univariate polynomial on reference element $I = [-1, 1]$ as $\mathscr{B}^e(\xi) \in \mathbb{P}^k(I)$ such that $\mathscr{B}^e(\xi)$ is an approximation of $\mathbf{B}(P^e(\xi)) \cdot \mathbf{n}$, where

$$P^e(\xi) = (x^e(\xi), y^e(\xi)) = \frac{1}{2}(1+\xi)P_{end} + \frac{1}{2}(1-\xi)P_{start}$$

is the linear mapping from I to e. Denote the collection $\mathscr{B} = \{\mathscr{B}^e\}_{e\in\mathscr{E}}$.

Then, introducing the notation $E_z(\mathbf{q}) = u_y B_x - u_x B_y$, we can rewrite the governing equation of B_x and B_y as

$$\frac{\partial B_x}{\partial t} + \frac{\partial E_z}{\partial y} = 0, \quad \frac{\partial B_y}{\partial t} - \frac{\partial E_z}{\partial x} = 0. \tag{2.7}$$

Therefore, we have

$$\frac{\partial\left(\mathbf{B}\cdot\mathbf{n}\right)}{\partial t} + \frac{\partial E_z}{\partial \mathbf{m}} = n_1\frac{\partial B_x}{\partial t} + n_2\frac{\partial B_y}{\partial t} + (-n_2)\frac{\partial E_z}{\partial x} + n_1\frac{\partial E_z}{\partial y} = 0. \tag{2.8}$$

Notice that (2.8) can be treated as a 1D problem along $\mathbf{m}$-direction, hence we can use it to update the 1D polynomial $\mathscr{B}^e(\xi)$. We want to remark that the edge e may belong to two cells, but we only compute $\mathbf{B}\cdot\mathbf{n}$ on e once via (2.8). And then we use it to reconstruct the magnetic field on these two cells such that the normal component is continuous across e.

Denote the numerical solution at time t^n as $\mathbf{q}_h^n = (\rho^n, (\rho\mathbf{u})^n, \mathcal{E}^n, \mathbf{B}^n)$ and $\mathscr{B}^n$. In general, the GDF framework in each Euler step from t^n to t^{n+1} can be summarized as the following steps:

Algorithm: Globally divergence-free method

Step 1 Compute $\tilde{\mathbf{q}}_h = (\rho^{n+1}, (\rho\mathbf{u})^{n+1}, \mathcal{E}^{n+1}, \tilde{\mathbf{B}}) \in \mathbf{V}_h^k$ from t^n to t^{n+1} by (2.5) in each cell.

Step 2 Update $\mathscr{B}^e$ on each edge by (2.8) from t^n to t^{n+1} to obtain $\mathscr{B}^{n+1} \in \mathbb{P}^k(e)$.

Step 3 Use the information of $\mathscr{B}^{n+1}$ and $\tilde{\mathbf{B}}$ to reconstruct a interior GDF magnetic field $\mathbf{B}^{n+1}$. Employ it to cover $\tilde{\mathbf{B}}$, then obtain $\mathbf{q}_h^{n+1} = (\rho^{n+1}, (\rho\mathbf{u})^{n+1}, \mathcal{E}^{n+1}, \mathbf{B}^{n+1}) \in \mathbf{V}_h^k$.

Moreover, it is worth noting that $\mathscr{B}$ must satisfy an additional constraint [5]. In a cell K, integrating the divergence-free condition of the exact solution yields

$$0 = \int_K \nabla \cdot \mathbf{B} \, \mathrm{d}K = \int_{\partial K} (\mathbf{B} \cdot \mathbf{n}) \, \mathrm{d}s, \tag{2.9}$$

which is a necessary condition of (2.3). Hence, the quantity $\mathscr{B}$ must satisfy the condition

$$\sum_{e \subset \partial K} \frac{|e|}{2} \int_{-1}^{1} \mathscr{B}^e(\xi) \, \mathrm{d}\xi = 0, \tag{2.10}$$

for all $K \in \mathcal{K}$. This is called the *cell-average constraint* in the following. The constraint (2.10) is naturally satisfied at initial, and should be preserved at each time step.

Next, we will discuss the evolution of $\mathscr{B}^e$ on each edge, and the GDF reconstruction in each cell in detail.

2.2.1 Constraint-preserving scheme for $\mathscr{B}^e$

In this subsection, we will discuss the updating scheme on each edge for the normal magnetic component $\mathscr{B}^e$. Since the B_z component is independent of the divergence condition in 2D cases, we will omit it, and use the notation $\mathbf{B} = (B_x, B_y)^T$ in this and next subsection for simplicity.

Again, consider an edge e with direction $\mathbf{m}$ and normal direction $\mathbf{n}$. Then, the semi-discrete scheme of (2.8) for normal component is given by: Find $\mathscr{B}^e(\xi) \in \mathbb{P}^k(I)$, such that for all $w(\xi) \in \mathbb{P}^k(I)$,

$$\frac{|e|}{2} \int_{-1}^{1} \frac{\partial \mathscr{B}^e}{\partial t} w \mathrm{d}\xi = \int_{-1}^{1} \widehat{E}_z \frac{\mathrm{d}w}{\mathrm{d}\xi} \mathrm{d}\xi - \widetilde{E}_z|_{P_{end}} \, w\left(1\right) + \widetilde{E}_z|_{P_{start}} \, w\left(-1\right). \tag{2.11}$$

Here, $\widehat{E}_z$ is the 1D numerical flux on the edge e, which is a single value obtained by two limiters to edge e. Moreover, $\widetilde{E}_z$ is the 2D numerical flux at vertices P_{start} and P_{end}, which are obtained based on several limited states at the vertices. In Fig. 2.2, we provide a schematic diagram of the notations at a vertex Λ. The cells in the anticlockwise and clockwise directions of an edge e are denoted by acw and cw, respectively. And for the DG scheme, a key point is the design of $\widehat{E}_z$ and $\widetilde{E}_z$.

In the finite volume method [41], the authors suggest to compute the 2D numerical flux $\widetilde{E}_z$ by

$$\widetilde{E}_z = \frac{1}{N_\Lambda} \sum_{\Lambda \in e} \left\{ \frac{1}{2} \left(E_z\left(\mathbf{q}^{cw}\right) + E_z\left(\mathbf{q}^{acw}\right) \right) - \alpha n_2 \left(B_x^{acw} - B_x^{cw} \right) \right\}, \tag{2.12}$$

which simply uses information of the 6th component in $\mathbf{F}$ and $\mathbf{q}$. N_Λ is the number of e satisfying $\Lambda \in e$. $\mathbf{q}^{cw,acw}$ are the limiting point values at Λ in the corresponding side

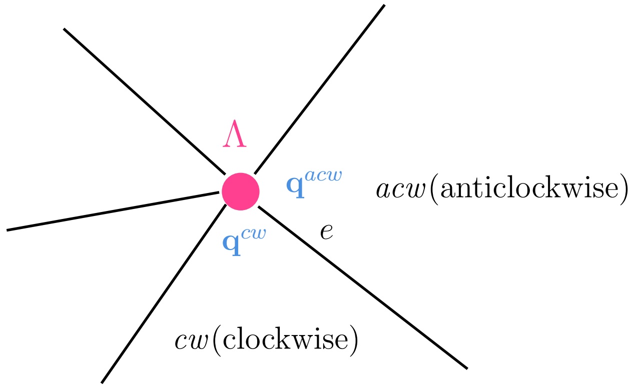

Figure 2.2. The notations around a vertex Λ.

cell of e. We remark here that in (2.12), the dissipation coefficient of LF flux is doubled from $\alpha/2$ to α to ensure stability [41, 19]. However, if we consider a situation where four cartesian zones come together at a vertex, this formulation only considers the vertical contribution, but misses the horizontal contribution. On the other hand, the FV scheme [41] only needs the 2D numerical flux at vertices, but for the DG scheme, we also need the 1D numerical flux $\widehat{E}_z$ on edges. If we extend the way of (2.12) to compute $\widehat{E}_z$, i.e.

$$\widehat{E}_z = \frac{1}{2}(E_z(\mathbf{q}^{cw}) + E_z(\mathbf{q}^{acw})) - \frac{\alpha}{2} n_2 (B_x^{acw} - B_x^{cw}), \tag{2.13}$$

the scheme may become unstable in some situations. This will be shown in the numerical experiments.

In this work, we redesign the formulation of $\widehat{E}_z$ and $\widetilde{E}_z$ for DG scheme. Let us begin from $\widehat{E}_z(\mathbf{q}^{cw}, \mathbf{q}^{acw}, \mathbf{n})$. In order to utilize both the horizontal and vertical contribution, we suggest the following three "consistent" principles:

1. When $\mathbf{n} = (\pm 1, 0)$, the flux function satisfies

$$\widehat{E}_z(\mathbf{q}^{cw}, \mathbf{q}^{acw}, \mathbf{n}) = \frac{1}{2}(E_z(\mathbf{q}^{cw}) + E_z(\mathbf{q}^{acw})) \pm \frac{\alpha}{2}(B_y^{acw} - B_y^{cw}). \tag{2.14}$$

2. When $\mathbf{n} = (0, \pm 1)$, the flux function satisfies

$$\widehat{E}_z(\mathbf{q}^{cw}, \mathbf{q}^{acw}, \mathbf{n}) = \frac{1}{2}(E_z(\mathbf{q}^{cw}) + E_z(\mathbf{q}^{acw})) \mp \frac{\alpha}{2}(B_x^{acw} - B_x^{cw}). \tag{2.15}$$

3. When $\mathbf{q}^{cw} = \mathbf{q}^{acw} = \mathbf{q}$, the flux function satisfies

$$\widehat{E}_z(\mathbf{q}, \mathbf{q}, \mathbf{n}) = E_z(\mathbf{q}). \tag{2.16}$$

The first and second conditions lead to consistency with the formulation on rectangular meshes [19], and the third condition results in consistency with the function E_z. We note here that the formulation (2.13) in [41] fails in the first two conditions. To satisfy these three conditions, we propose the following formulation for $\widehat{E}_z$:

$$\widehat{E}_z(\mathbf{q}^{cw}, \mathbf{q}^{qcw}, \mathbf{n}) = n_2\mathbf{h}_6(\mathbf{q}^{cw}, \mathbf{q}^{acw}, \mathbf{n}) - n_1\mathbf{h}_7(\mathbf{q}^{cw}, \mathbf{q}^{acw}, \mathbf{n}), \tag{2.17}$$

where $\mathbf{h}_6$ and $\mathbf{h}_7$, respectively, correspond to the 6th and 7th components of $\mathbf{h}$ in (2.6). Specifically,

$$\begin{aligned}\widehat{E}_z =& n_2\mathbf{h}_6\left(\mathbf{q}^{cw}, \mathbf{q}^{acw}, \mathbf{n}\right) - n_1\mathbf{h}_7\left(\mathbf{q}^{cw}, \mathbf{q}^{acw}, \mathbf{n}\right)\\ =& n_2\left[\frac{1}{2}\left(E_z\left(\mathbf{q}^{cw}\right) + E_z\left(\mathbf{q}^{acw}\right)\right)n_2 - \frac{1}{2}\alpha\left(B_x^{acw} - B_x^{cw}\right)\right]\\ &- n_1\left[\frac{1}{2}\left(-E_z\left(\mathbf{q}^{cw}\right) - E_z\left(\mathbf{q}^{acw}\right)\right)n_1 - \frac{1}{2}\alpha\left(B_y^{acw} - B_y^{cw}\right)\right]\\ =& \frac{1}{2}\left(n_1^2 + n_2^2\right)\left(E_z\left(\mathbf{q}^{cw}\right) + E_z\left(\mathbf{q}^{acw}\right)\right) + \frac{\alpha}{2}\left[-n_2\left(B_x^{acw} - B_x^{cw}\right) + n_1\left(B_y^{acw} - B_y^{cw}\right)\right]\\ =& \frac{1}{2}\left(E_z(\mathbf{q}^{cw}) + E_z(\mathbf{q}^{acw})\right) + \frac{\alpha}{2}\mathbf{m}\cdot\left(\mathbf{B}^{acw} - \mathbf{B}^{cw}\right).\end{aligned} \tag{2.18}$$

It is easy to verify that (2.18) satisfies (2.14) to (2.16). Based on this, we compute the 2D flux $\widetilde{E}_z$ by

$$\widetilde{E}_z = \frac{1}{N_\Lambda}\sum_{\Lambda\in e}\left\{\frac{1}{2}\left(E_z\left(\mathbf{q}^{cw}\right) + E_z\left(\mathbf{q}^{acw}\right)\right) + \alpha\mathbf{m}\cdot\left(\mathbf{B}^{acw} - \mathbf{B}^{cw}\right)\right\}. \tag{2.19}$$

The design of scheme (2.11) with numerical fluxes (2.18) and (2.19) is one of the main contributions in this paper. In the numerical experiments, we will show that this modification can improve the stability of the scheme.

Moreover, for scheme (2.11), we can prove that $\mathscr{B}^e$ around a cell K satisfies the cell-average constraint.

Theorem 2.1. *For a cell K shown in Fig 2.1, the scheme (2.11) satisfies the cell-average constraint in the sense of*

$$\frac{\mathrm{d}}{\mathrm{d}t}\left(\sum_{i=1}^{3}\frac{|e_i|}{2}\int_{-1}^{1}\mathscr{B}^{e_i}(\xi)\,\mathrm{d}\xi\right) = 0. \tag{2.20}$$

Proof. Taking $w = 1$ in (2.11) for each edge e_1, e_2, e_3, we can get

$$\begin{aligned}\frac{|e_1|}{2}\int_{-1}^{1}\frac{\partial\mathscr{B}^{e_1}}{\partial t}\,\mathrm{d}\xi &= \widetilde{E}_z|_{P_3} - \widetilde{E}_z|_{P_2},\\ \frac{|e_2|}{2}\int_{-1}^{1}\frac{\partial\mathscr{B}^{e_2}}{\partial t}\,\mathrm{d}\xi &= \widetilde{E}_z|_{P_1} - \widetilde{E}_z|_{P_3},\end{aligned}$$

$$\frac{|e_3|}{2}\int_{-1}^{1}\frac{\partial \mathscr{B}^{e_3}}{\partial t}\,\mathrm{d}\xi = \widetilde{E}_z|_{P_2} - \widetilde{E}_z|_{P_1}.$$

Summing all these together yields (2.20). □

2.2.2 The least-squares reconstruction

Utilizing the magnetic field computed by (2.5) and the normal magnetic components by (2.11), we are aiming to determine an interior GDF magnetic field $\mathbf{B}_h \in [V_h^k]^2$. Mathematically, the reconstruction problem on a cell K is given by: Find an interior magnetic field $\mathbf{B}^{rec} \in [\mathbb{P}^k(K)]^2$, such that

$$\nabla \cdot \mathbf{B}^{rec} = 0 \quad \text{in} \quad K, \tag{2.21}$$

$$\mathbf{B}^{rec}(x^{e_i}(\xi), y^{e_i}(\xi)) \cdot \mathbf{n}_i = \mathscr{B}^{e_i}(\xi) \quad \text{on} \quad I, \quad i = 1,2,3. \tag{2.22}$$

For the approximation$[\mathbb{P}^k]^2$, it can be verified that the DOFs N_d and number of conditions N_c of the above reconstruction problem respectively are

$$N_d = (k+1)(k+2), \quad N_c = 3(k+1) + \frac{k(k+1)}{2} - 1.$$

Here we note that the cell-average constraint can reduce one condition [5, 28]. It can be verified that $N_d \geq N_c$ holds for any $k \in \mathbb{N}$. Hence, the reconstruction problem is solvable for arbitrary approximation $[\mathbb{P}^k]^2$, but only uniquely determined for $k = 0, 1$. It is worth noting that there is a point differ from rectangular meshes: For rectangular meshes, the number of conditions N_c is larger than the DOFs of $[\mathbb{P}^k]^2$, thus we need to utilize $[\mathbb{P}^{k+1}]^2$ as the interior magnetic field to match the number of conditions [5]. But for triangular meshes, using the space $[\mathbb{P}^k]^2$ is sufficient.

For $k \geq 2$, there are extra DOFs to be determined. A natural way is to determine these extra DOFs in the least-squares sense, which was first introduced in the finite volume method [3]. However, the linear system of the least-squares equation in [3] depends on the geometry of a specific mesh, which may lead to issues of storage and computational efficiency for non-uniform meshes or moving meshes. To address this, we will construct a cell-independent least-squares reconstruction, which is unified for arbitrary k, and does not rely on the specific form of the basis functions.

At first, we give a brief review of the geometric transformations between the physical cell K in Fig. 2.1 and reference cell K_0 defined as

$$K_0 = \{(X,Y) : \ X \geq 0, \ Y \geq 0, \ X + Y \leq 1\},$$

with $P_1^0 = (1,0), \ P_2^0 = (0,1), \ P_3^0 = (0,0)$. The linear mapping $\mathscr{N} : (x,y) \to (X,Y)$ is given by

$$X = \frac{1}{\Sigma_K}\begin{vmatrix} 1 & x & y \\ 1 & x_2 & y_2 \\ 1 & x_3 & y_3 \end{vmatrix}, \quad Y = \frac{1}{\Sigma_K}\begin{vmatrix} 1 & x_1 & y_1 \\ 1 & x & y \\ 1 & x_3 & y_3 \end{vmatrix}, \quad \Sigma_K = \begin{vmatrix} 1 & x_1 & y_1 \\ 1 & x_2 & y_2 \\ 1 & x_3 & y_3 \end{vmatrix},$$

which satisfies $\mathcal{N}(P_i) = P_i^0,\ i = 1, 2, 3$. It can be derived that the Jacobian of $\mathcal{N}$ is

$$\mathcal{D} := \frac{\partial \mathcal{N}(x,y)}{\partial(x,y)} = \frac{1}{\Sigma_K}\begin{bmatrix} y_2 - y_3 & x_3 - x_2 \\ y_3 - y_1 & x_1 - x_3 \end{bmatrix} =: \frac{1}{\Sigma_K}\begin{bmatrix} A & B \\ C & D \end{bmatrix}.$$

Suppose the basis functions of $\mathbb{P}^k$ in K_0 are $\{\phi_l\}_{l=1}^d,\ d = (k+1)(k+2)/2$. Then, the l-th basis function on a cell K can be represented by

$$\phi_l^K(x,y) := \phi_l(\mathcal{N}(x,y)) = \phi_l(X(x,y), Y(x,y)), \quad l = 1, \cdots, d.$$

Moreover, by the chain rule, we have

$$\frac{\partial \phi_l^K(x,y)}{\partial x} = \frac{\partial \phi_l(X,Y)}{\partial X}\frac{\partial X}{\partial x} + \frac{\partial \phi_l(X,Y)}{\partial Y}\frac{\partial Y}{\partial x} = \frac{1}{\Sigma_K}\left[A\frac{\partial \phi_l}{\partial X}(X,Y) + C\frac{\partial \phi_l}{\partial Y}(X,Y)\right],$$

$$\frac{\partial \phi_l^K(x,y)}{\partial y} = \frac{\partial \phi_l(X,Y)}{\partial X}\frac{\partial X}{\partial y} + \frac{\partial \phi_l(X,Y)}{\partial Y}\frac{\partial Y}{\partial y} = \frac{1}{\Sigma_K}\left[B\frac{\partial \phi_l}{\partial X}(X,Y) + D\frac{\partial \phi_l}{\partial Y}(X,Y)\right].$$

Now we introduce some matrices will be used later. Assume there are sufficient many quadrature points $\{P_m^G\}_{m=1}^{N_G}$ inside K_0 with weight ω_m^G, and 1D quadrature points on each edge of K_0 by $\{P_m^{G,i}\}_{m=1,i=1}^{n_G,3}$. Then, the metric terms are defined by

$$\Phi(m;l) = \phi_l(P_m^G), \quad \Phi_X(m;l) = \frac{\partial \phi_l}{\partial X}(P_m^G), \quad \Phi_Y(m;l) = \frac{\partial \phi_l}{\partial Y}(P_m^G).$$

$$\Phi_i(m;l) = \phi_l(P_m^{G,i}), \quad i = 1, 2, 3,$$

and further construct the matrices

$$\mathbf{\Phi}, \mathbf{\Phi}_X, \mathbf{\Phi}_Y \in \mathbb{R}^{N_G \times d}, \quad \mathbf{\Phi}_i \in \mathbb{R}^{n_G \times d},\ i = 1, 2, 3.$$

Moreover, the mass matrix is defined by

$$\mathbf{M} = \mathbf{\Phi}^T \mathbf{W} \mathbf{\Phi}, \quad \mathbf{W} = \mathrm{diag}\{\omega_1^G, \cdots, \omega_{N_G}^G\}, \quad \mathbf{M}_2 = \mathrm{diag}\{\mathbf{M}, \mathbf{M}\}.$$

It is worth noting that all above matrices rely only on the information of K_0, but are independent of K. Assume that

$$B_x^{rec} = a_1\phi_1^K + \cdots + a_d\phi_d^K, \quad B_y^{rec} = b_1\phi_1^K + \cdots + b_d\phi_d^K,$$

and denote $\mathbf{a} = (a_1, \cdots, a_d)^T$, $\mathbf{b} = (b_1, \cdots, b_d)^T$. Then, the divergence on the interior quadrature points can be calculated by

$$\nabla \cdot \mathbf{B}^{rec}(P_m^G) = \frac{1}{\Sigma_K} \sum_{l=1}^{d} \left[A\Phi_X(m;l) + C\Phi_Y(m;l)\right] a_l + \left[B\Phi_X(m;l) + D\Phi_Y(m;l)\right] b_l. \tag{2.23}$$

Since the quadrature is exact for $\mathbb{P}^k$ polynomials, (2.21) is equivalent to

$$(A\mathbf{\Phi}_X + C\mathbf{\Phi}_Y)\mathbf{a} + (B\mathbf{\Phi}_X + D\mathbf{\Phi}_Y)\mathbf{b} = \mathbf{0}.$$

Besides, the values of normal component $\mathscr{B}^{e_i}$ on $\{P_m^{G,i}\}_{m=1}^{n_G}$ are denoted by a column vector $\boldsymbol{\mathcal{B}}_i$. Then similarly, (2.22) is equivalent to

$$[\mathbf{\Phi}_i\mathbf{a} \quad \mathbf{\Phi}_i\mathbf{b}]\,\mathbf{n}_i = \boldsymbol{\mathcal{B}}_i, \quad i = 1, 2, 3. \tag{2.24}$$

Then, combining (2.23) and (2.24), we can obtain a linear system. However, it seems the system relies on the geometry of K. In order to obtain a cell-independent form, the key is to represent the normal vectors in the following form

$$\mathbf{n}_1 = -\frac{1}{|e_1|}(A, B)^T, \ \mathbf{n}_2 = -\frac{1}{|e_2|}(C, D)^T, \ \mathbf{n}_3 = \frac{1}{|e_3|}(A + C, B + D)^T.$$

Therefore, the linear system combined by (2.23) and (2.24) can be written as

$$\begin{bmatrix} A\mathbf{\Phi}_X + C\mathbf{\Phi}_Y & B\mathbf{\Phi}_X + D\mathbf{\Phi}_Y \\ A\mathbf{\Phi}_1 & B\mathbf{\Phi}_1 \\ C\mathbf{\Phi}_2 & D\mathbf{\Phi}_2 \\ (A + C)\,\mathbf{\Phi}_3 & (B + D)\,\mathbf{\Phi}_3 \end{bmatrix} \begin{bmatrix} \mathbf{a} \\ \mathbf{b} \end{bmatrix} = \begin{bmatrix} \mathbf{0} \\ -|e_1|\,\boldsymbol{\mathcal{B}}_1 \\ -|e_2|\,\boldsymbol{\mathcal{B}}_2 \\ |e_3|\,\boldsymbol{\mathcal{B}}_3 \end{bmatrix}. \tag{2.25}$$

Introduce the following variable substitution

$$\boldsymbol{\alpha} = A\mathbf{a} + B\mathbf{b}, \quad \boldsymbol{\beta} = C\mathbf{a} + D\mathbf{b},$$

then we have

$$\begin{bmatrix} \mathbf{\Phi}_X & \mathbf{\Phi}_Y \\ \mathbf{\Phi}_1 & O \\ O & \mathbf{\Phi}_2 \\ \mathbf{\Phi}_3 & \mathbf{\Phi}_3 \end{bmatrix} \begin{bmatrix} \boldsymbol{\alpha} \\ \boldsymbol{\beta} \end{bmatrix} = \begin{bmatrix} \mathbf{0} \\ -|e_1|\,\boldsymbol{\mathcal{B}}_1 \\ -|e_2|\,\boldsymbol{\mathcal{B}}_2 \\ |e_3|\,\boldsymbol{\mathcal{B}}_3 \end{bmatrix}. \tag{2.26}$$

Denote (2.26) as $\mathbf{H}\mathbf{z} = \boldsymbol{\zeta}$. This system has a unique solution for $k = 0, 1$. For $k \geq 2$, to determine a unique solution of (2.26), we are aiming to solve the optimization problem

$$\min_{\mathbf{z}} \|\mathbf{z} - \tilde{\mathbf{z}}\|^2_{\mathbf{M}_2}, \quad \text{s.t.} \ \ \mathbf{H}\mathbf{z} = \boldsymbol{\zeta}, \tag{2.27}$$

where $\|\mathbf{z}\|^2_{\mathbf{M}_2} = \mathbf{z}^T \mathbf{M}_2 \mathbf{z}$,

$$\tilde{\mathbf{z}} = \begin{bmatrix} \tilde{\boldsymbol{\alpha}} \\ \tilde{\boldsymbol{\beta}} \end{bmatrix}, \quad \tilde{\boldsymbol{\alpha}} = A\tilde{\mathbf{a}} + B\tilde{\mathbf{b}}, \quad \tilde{\boldsymbol{\beta}} = C\tilde{\mathbf{a}} + D\tilde{\mathbf{b}},$$

and $\tilde{\mathbf{B}} = \left(\sum_{l=1}^{d} \tilde{a}_l \phi_l^K, \sum_{l=1}^{d} \tilde{b}_l \phi_l^K \right)$ is magnetic field computed by (2.5).

Next, we provide a method to solve (2.27), which is also used in the nodal DG framework [27]. Assume the singular value decomposition of $\mathbf{H}$ is $\mathbf{H} = \mathbf{U}\mathbf{S}\mathbf{V}^T$, where

$$\mathbf{U} \in \mathbb{R}^{(N_G + 3n_G) \times r}, \quad \mathbf{S} \in \mathbb{R}^{r \times r}, \quad \mathbf{V} \in \mathbb{R}^{2d \times r}, \quad r = \text{rank}(\mathbf{H}).$$

Then we can rewrite (2.26) as

$$\mathbf{S}\mathbf{V}^T \mathbf{z} = \mathbf{U}^T \boldsymbol{\zeta}. \tag{2.28}$$

Denote it by

$$\mathbf{H}_1 \mathbf{z} = \boldsymbol{\zeta}_1. \tag{2.29}$$

Then the solution of (2.27) can be obtained by solving the following linear system

$$\begin{bmatrix} \mathbf{M}_2 & \mathbf{H}_1^T \\ \mathbf{H}_1 & O \end{bmatrix} \begin{bmatrix} \mathbf{z} \\ \boldsymbol{\lambda} \end{bmatrix} = \begin{bmatrix} \mathbf{M}_2 \tilde{\mathbf{z}} \\ \boldsymbol{\zeta}_1 \end{bmatrix}, \tag{2.30}$$

where $\boldsymbol{\lambda}$ is the Lagrange multiplier. Since $\mathbf{H}_1$ is of full row rank, (2.30) has a unique solution. Denote the inverse of the above coefficient matrix by

$$\mathbf{G} = \begin{bmatrix} \mathbf{G}_1 & \mathbf{G}_2 \\ \mathbf{G}_3 & \mathbf{G}_4 \end{bmatrix},$$

then the explicit solution of (2.30) is

$$\mathbf{z} = \mathbf{G}_1\mathbf{M}_2\tilde{\mathbf{z}} + \mathbf{G}_2\boldsymbol{\zeta}_1. \tag{2.31}$$

Notice that the elements of $\mathbf{G}$ only depend on the values and derivatives of basis functions at several quadrature points on the reference triangle K_0, but not the information of K. For any given basis functions and the quadrature rules, we can save the inverse matrix $\mathbf{G}$ only once in numerical implementation before the computation, then the algorithm can be realized by just a matrix multiply for every cell $K \in \mathcal{K}$, instead of solving the linear system (2.30). In particular, this will significantly reduce the computational cost and storage requirements for non-uniform meshes and moving meshes [3].

Remark 2.1. *Different from the original least-squares reconstruction in [3], we introduce the auxiliary variable* $\boldsymbol{\alpha}, \boldsymbol{\beta}$*,*

$$\begin{bmatrix} \alpha_l \\ \beta_l \end{bmatrix} = \Sigma_K \mathcal{D} \begin{bmatrix} a_l \\ b_l \end{bmatrix}, \quad l = 1, \cdots, d,$$

and try to solve the system (2.26)*. In fact, our optimization problem* (2.27) *does not minimize the standard* L^2 *norm of* $\mathbf{B}^{rec} - \tilde{\mathbf{B}}$*. Instead, it focuses on minimizing the* L^2 *norm of* $\mathcal{D}(\mathbf{B}^{rec} - \tilde{\mathbf{B}})$*. Despite this modification, the approach successfully maintains both accuracy and the GDF property.*

2.3 The jump filter

For problems containing strong shocks, a limiter should be added to suppress spurious oscillations. In this paper, we apply a simplified jump filter [39] to the solution. The original version is designed for rectangular meshes, here we perform a straightforward extension and apply it to triangular meshes.

For a cell K, the conservative variables are modified by

$$\mathbf{q}_h^{(mod)}|_K = \overline{\mathbf{q}}_K + \theta_K \left(\mathbf{q}_h|_K - \overline{\mathbf{q}}_K \right). \tag{2.32}$$

Here, $\overline{\mathbf{q}}_K$ is the cell average, and $\mathbf{q}_h^{(mod)}$ denotes the modified numerical solution. The parameter $\theta_K = \exp(-\sigma_K \Delta t) \in [0,1]$ with $\sigma_K = \max\limits_{1 \le m \le 8} \sigma_K^m$,

$$\sigma_K^m = c_f \int_{\partial K} \frac{1}{h_K} |[q^{(m)}]| + 2\left(|[q_x^{(m)}]| + |[q_y^{(m)}]| \right) \mathrm{d}s, \quad c_f = c_0 \frac{\overline{\rho}_K \alpha_K}{\overline{\mathcal{E}}_K + \overline{p}_K^\star},$$

and h_K is the diameter of K. $q^{(m)}$ is the m-th component of $\mathbf{q}_h$. $[w]$ is the jump of a function w on the edge. α_K is the local absolutely maximal wave speed in cell K. Meanwhile, c_0 is a free parameter, a suggested range is $0.01 \le c_0 \le 1$.

For the GDF method, an additional limiting step should be applied to $\mathscr{B}$ on interfaces. Similar to [5, 27, 28], we first limit the interior solution $\mathbf{q}_h$ in each K by (2.32), simultaneously obtaining the limiting coefficient θ_K for each cell. Subsequently, the normal magnetic component $\mathscr{B}^e$ can be effectively limited by

$$\mathscr{B}^{e,(mod)} = \overline{\mathscr{B}}^e + \theta_e(\mathscr{B}^e - \overline{\mathscr{B}}^e), \quad \text{with} \quad \theta_e = \min\{\theta_K : e \subset \partial K\}. \tag{2.33}$$

The limiting step (2.32) and (2.33) should be formulated before the reconstruction step (2.27), i.e., added between **Step 2** and **Step 3** in **Algorithm**. Since (2.33) does not change the cell-average of $\mathscr{B}^e$, the cell-average constraint (2.10) still holds [27]. Consequently, this approach maintains the GDF property for the reconstructed interior magnetic field.

3 Numerical experiments

In this section, we simulate the ideal MHD equation to verify the accuracy, efficiency, and stability of our scheme. We use the CFL condition

$$\Delta t = \text{CFL} \cdot \frac{h_{min}}{\alpha_\Omega}, \quad \text{CFL} = \frac{1}{2k+1},$$

for all tests, where α_Ω is an estimate of global maximal wave speed. Without special declaration, we only present the results of $k = 2$ of the proposed GDF DG method. The jump filter introduced in Section 2.3 is applied for all tests.

For some problems, we will also compare the performance of the proposed GDF method with the standard DG method (denoted by "Base") and LDF method on the same meshes and parameters.

Furthermore, we study the divergence in each cell K measured by [12]

$$\|\text{div}\mathbf{B}\|_K = \int_K |\nabla \cdot \mathbf{B}| \, \mathrm{d}K + \int_{\partial K} |[\mathbf{B} \cdot \mathbf{n}]| \, \mathrm{d}s,$$

and the total divergence norm on Ω defined by

$$\|\text{div}\mathbf{B}\| = \frac{1}{|\Omega|} \sum_{K \in \mathcal{K}} \|\text{div}\mathbf{B}\|_K .$$

It is clear that for GDF method, the quantity $\|\text{div}\mathbf{B}\|$ is expected to be at machine level. And in [12], it is discussed that for Base scheme and LDF scheme, an expected result is $\|\text{div}\mathbf{B}\| = \mathcal{O}(h^k)$ for smooth solutions.

Example 3.1. ***(Smooth MHD vortex.)***

First, we consider the MHD vortex problem to test the accuracy of our scheme, which is originally introduced by Shu [36] in the hydrodynamical system, and was extended to MHD equations by Balsara [1]. The computational domain is set as $\Omega = [-10, 10] \times [-10, 10]$ with periodic boundary conditions in each direction. The initial data is a steady flow with a perturbation:

$$(\rho, u_x, u_y, u_z, B_x, B_y, B_z, p) = (1, 1 + \delta u_x, 1 + \delta u_y, 0, \delta B_x, \delta B_y, 0, 1 + \delta p).$$

The perturbation satisfies

$$(\delta u_x, \delta u_y) = \frac{\eta}{2\pi} \hat{\nabla} \times \exp\left\{0.5\left(1 - r^2\right)\right\},$$

$$(\delta B_x, \delta B_y) = \frac{\xi}{2\pi} \hat{\nabla} \times \exp\left\{0.5\left(1 - r^2\right)\right\},$$

$$\delta p = \left(\xi^2\left(1 - r^2\right) - \eta^2\right) \frac{1}{8\pi^2} \exp\left(1 - r^2\right),$$

where $\hat{\nabla} \times w := (\partial_y w, -\partial_x w)$, and $r^2 = x^2 + y^2$. We take $\eta = \xi = 1$ in computation. The exact solution is the initial condition propagates with a velocity of $(1, 1)$.

We run this problem until $T = 20$ with $k = 2, 3, 4$. A sample mesh is shown in Fig 3.3. The L^2 errors and orders of B_x are presented in Table 3.1. It can be seen that for all $k = 2, 3, 4$, the Base scheme shows the loss of accuracy, especially for $k = 4$. Meanwhile, the LDF and GDF schemes could maintain the designed $(k + 1)$-th accuracy.

Moreover, the divergence norms and orders are shown in Table 3.2, and similar situations have also occurred in the Base scheme. Besides, the divergence norm of LDF scheme achieves k-th order, and the GDF scheme exactly preserves the divergence norm at machine level. We want to remark here that the loss of accuracy in Base scheme can also be found in [23]. To further analyze this phenomenon, we present the evolution of divergence norm in Fig. 3.4 of different schemes with mesh refinement from $N = 15372$ (denoted by 15K) to $N = 60204$ (denoted by 60K) for $k = 4$. As time increases, the divergence of the Base scheme demonstrates a loss of order accuracy, while the LDF scheme maintains the accuracy well, and the GDF scheme maintains the divergence at machine error level.

Example 3.2. ***(Magnetic field loop.)***

We consider the magnetic field loop test [20] to show the stability of our scheme, and use the same setup in [26]. The computational domain is $\Omega = [-1, 1] \times [-0.5, 0.5]$ with periodic boundary condition. The initial data is given by

$$(\rho, u_x, u_y, u_z, B_z, p) = (1, 2, 1, 1, 0, 1),$$

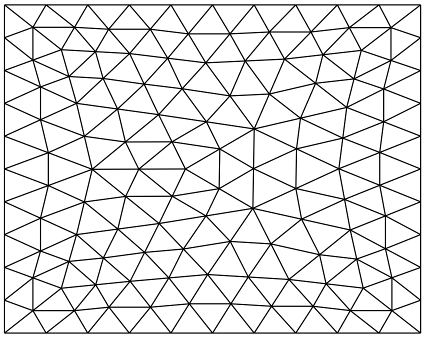

Figure 3.3. Example 3.1: A Sample of mesh.

Table 3.1. Example 3.1: Smooth MHD vortex. L^2 errors and orders of B_x at $T = 20$.

N	Base	Order	LDF	Order	GDF	Order
			$k = 2$			
1,100	6.57E-04	–	6.04E-04	–	1.41E-03	–
4,004	1.53E-04	2.10	4.49E-05	3.75	2.11E-04	2.74
15,372	3.79E-05	2.01	4.67E-06	3.27	2.99E-05	2.82
60,204	8.49E-06	2.16	7.41E-07	2.66	4.03E-06	2.89
			$k = 3$			
1,100	1.82E-04	–	8.55E-05	–	2.24E-04	–
4,004	1.51E-05	3.59	3.68E-06	4.54	7.74E-06	4.86
15,372	2.15E-06	2.81	1.51E-07	4.61	2.86E-07	4.76
60,204	3.20E-07	2.75	7.89E-09	4.26	1.11E-08	4.69
			$k = 4$			
1,100	3.61E-05	–	1.23E-05	–	2.39E-05	–
4,004	3.96E-06	3.19	3.23E-07	5.25	5.73E-07	5.38
15,372	3.65E-07	3.44	9.00E-09	5.17	1.31E-08	5.45
60,204	6.94E-08	2.39	2.78E-10	5.02	3.67E-10	5.16

and

$$(B_x, B_y) = \hat{\nabla} \times A_z, \quad A_z = \begin{cases} A_0\left(R - r\right), & r \le R, \\ 0, & r > R, \end{cases}$$

where $A_0 = 10^{-3}$, $R = 0.3$, $r = \sqrt{x^2 + y^2}$. To clearly show the instability of the formulation by Xu et al. [41] (denoted by "GDF-Xu"), we use a special uniform mesh for this example. A sample of mesh is shown in Fig. 3.5.

We simulate this problem until $T = 2$. In Fig. 3.6, we present the numerical solution of $\sqrt{B_x^2 + B_y^2}$ on $N = 128 \times 64 \times 2 = 16384$ uniform meshes with different schemes at the final time. For the Base scheme, the solution left non-physical traces during its movement [38]. And for the GDF-Xu scheme, since their formulation does not consider

Table 3.2. Example 3.1: Smooth MHD vortex. Divergence norm at $T = 20$.

N	Base	Order	LDF	Order	GDF	Order
$k = 2$						
1,100	1.29E-03	–	2.61E-04	–	2.68E-16	–
4,004	5.77E-04	1.16	8.14E-05	1.68	7.01E-16	–
15,372	2.26E-04	1.35	2.29E-05	1.83	1.84E-15	–
60,204	8.64E-05	1.39	5.77E-06	1.99	5.03E-15	–
$k = 3$						
1,100	5.08E-04	–	4.56E-05	–	3.55E-16	–
4,004	8.11E-05	2.65	4.69E-06	3.28	8.68E-16	–
15,372	1.97E-05	2.04	4.55E-07	3.37	2.26E-15	–
60,204	6.11E-06	1.69	5.45E-08	3.06	6.05E-15	–
$k = 4$						
1,100	8.53E-05	–	4.83E-06	–	4.16E-16	–
4,004	1.48E-05	2.53	3.23E-07	3.90	9.66E-16	–
15,372	2.42E-06	2.61	2.14E-08	3.92	2.54E-15	–
60,204	1.30E-06	0.90	1.37E-09	3.97	6.76E-15	–

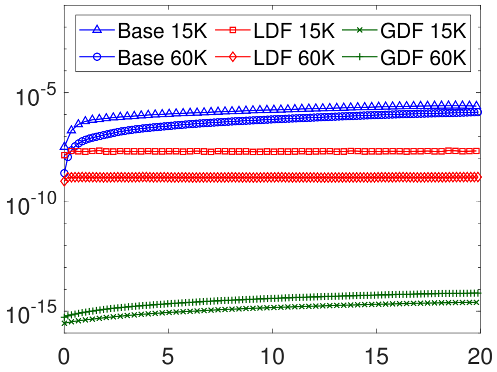

Figure 3.4. Example 3.1: Smooth MHD vortex. The time evolution of divergence norm with mesh refinement.

the horizontal jumps of the solution, it can be seen that the result shows a strong instability. Meanwhile, both the LDF scheme and the proposed GDF scheme give well-resolved results. However, our GDF scheme has better performance in preserving the structure of the magnetic field.

Example 3.3. ***(Orszag-Tang vortex.)***

We consider the Orszag-Tang problem [32], which is a widely used test example in the literature due to the complex interaction between several shocks generated as the whole system evolves. The computational domain is set as $\Omega = [0, 2\pi] \times [0, 2\pi]$ with

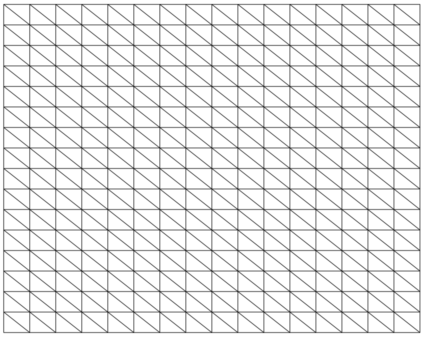

Figure 3.5. Example 3.2: A sample of uniform mesh.

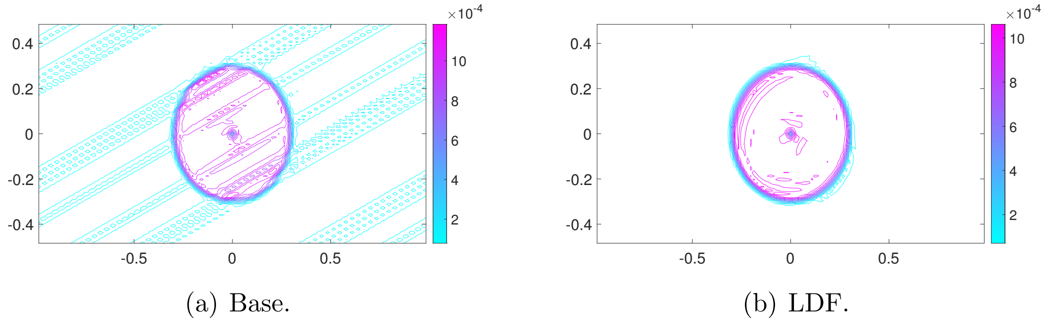

(a) Base.

(b) LDF.

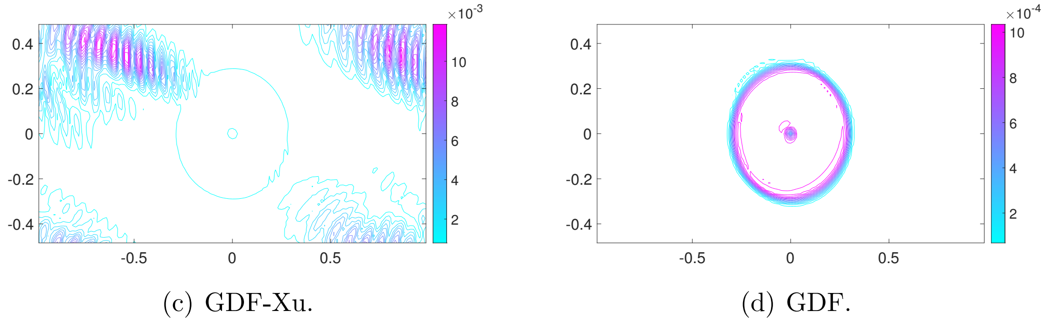

(c) GDF-Xu.

(d) GDF.

Figure 3.6. Example 3.2: Magnetic field loop. Numerical solution of $\sqrt{B_x^2 + B_y^2}$ of different schemes at $T = 2$. 15 contour lines are used.

periodic boundary conditions. And the initial data is given by

$$(\rho, u_x, u_y, u_z, B_x, B_y, B_z, p) = (\gamma^2, -\sin x, \sin y, 0, -\sin x, \sin 2y, 0, \gamma).$$

The mesh is the same to Fig. 3.3. Using $N = 152988$ cells with $h_{max} = 0.0324$, the results at $T = 0.5, 2, 3, 4$ are shown in Fig. 3.7. One can see that in the early stage, the solution is quite smooth. At $T = 2$, shocks have already appeared. At later times, the shocks interact with each other and the structure gets quite complicated, and the GDF scheme simulates these processes well. We also note here that the Base scheme will blow up before $T = 3$, and the LDF and GDF schemes can simulate stably. In Fig. 3.8, we compare the divergence at $T = 3$ for LDF and GDF schemes. It can be seen that for LDF scheme, although the interior divergence is zero, the jump of normal magnetic component near discontinuity is still very large.

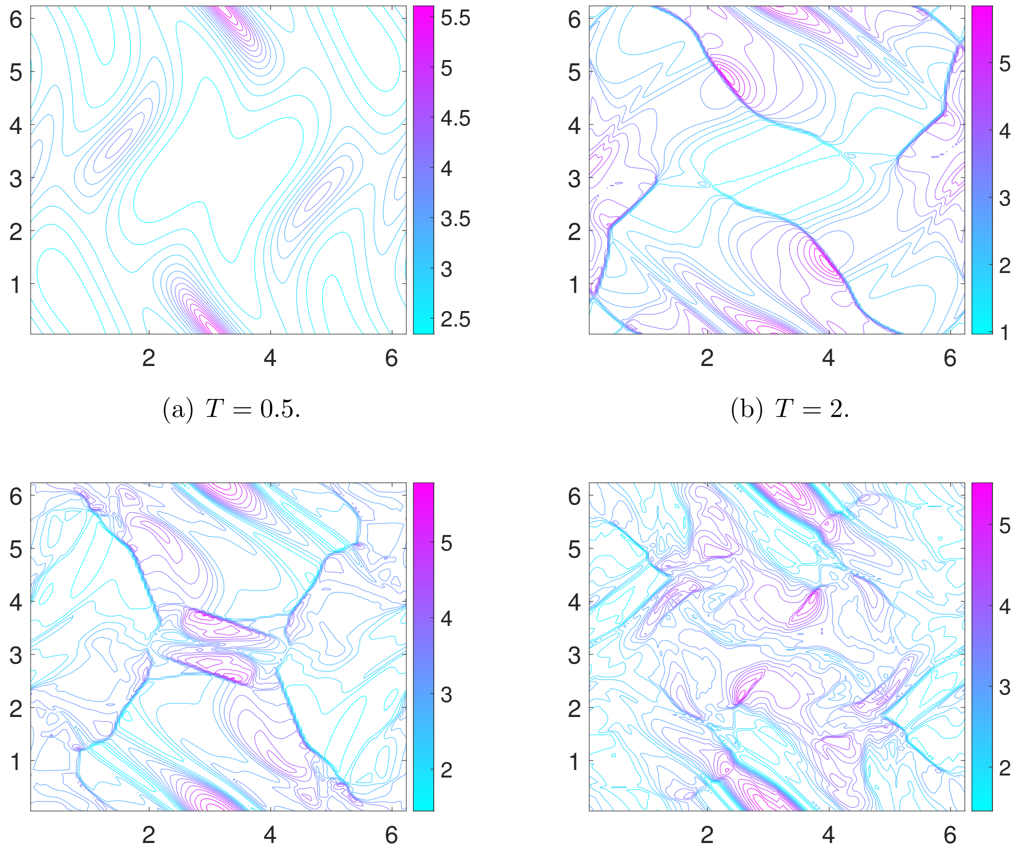

(a) $T = 0.5$.

(b) $T = 2$.

(c) $T = 3$.

(d) $T = 4$.

Figure 3.7. Example 3.3: Orszag-Tang vortex. The results of density on $N = 152988$ meshes. 15 contour lines are used.

Example 3.4. *(Rotor.)*

We consider the rotor problem originally presented by Balsara [6], and follow the setup in [37]. This test example involves a dense fluid disc rotating at the center while the surrounding fluid remains stationary. The magnetic field encircles the rotating dense fluid, transforming it into an oblate formation. In [24], it is demonstrated that insufficient control of magnetic field divergence errors in numerical schemes can result in observable Mach number distortions.

The computational domain is taken as a disk

$$\Omega = \{(x, y) : (x - 0.5)^2 + (y - 0.5)^2 \leq 0.65^2\}$$

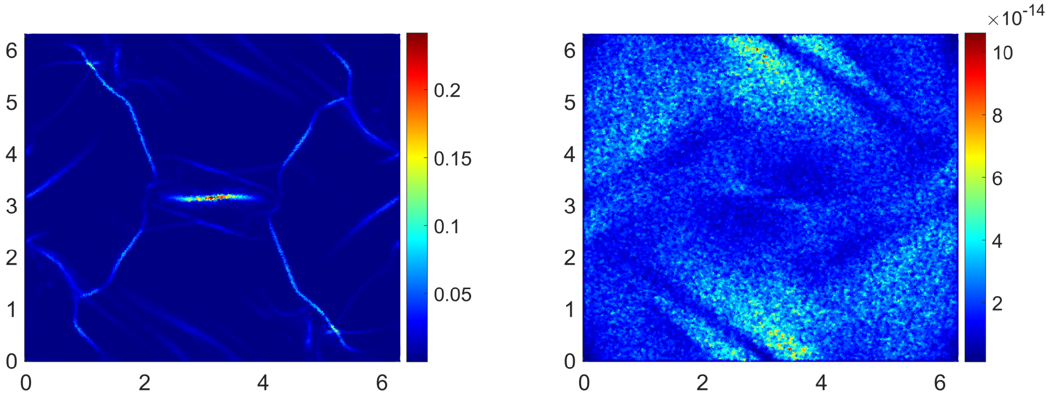

(a) LDF. (b) GDF.

Figure 3.8. Example 3.3: Orszag-Tang vortex. The divergence of different schemes at $T = 3$ on $N = 152988$ meshes.

instead of the original setup $\Omega = [0, 1] \times [0, 1]$. Outflow boundary condition is imposed on $\partial\Omega$. The initial data is given by

$$(\rho, u_x, u_y) = \begin{cases} (10, -(y-0.5)/r_0, (x-0.5)/r_0), & r < r_0, \\ (1+9f, -f(y-0.5)/r, f(x-0.5)/r), & r_0 < r < r_1, \\ (1, 0, 0), & r > r_1, \end{cases}$$

where

$$r = \sqrt{(x-0.5)^2 + (y-0.5)^2},\ r_1 = 0.115,\ r_0 = 0.1,\ f = \frac{(r_1 - r)}{(r_1 - r_0)},$$

and $p = 0.5,\ u_z = B_y = B_z = 0,\ B_x = 2.5/\sqrt{4\pi}$. A sample of mesh is shown in Fig. 3.9.

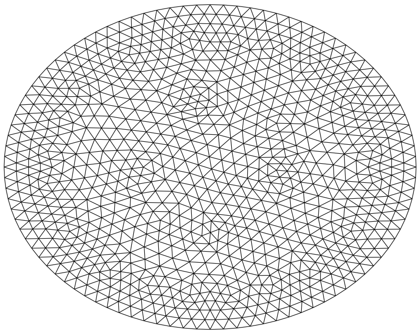

Figure 3.9. Example 3.4: Rotor. A Sample mesh.

We run this problem on $N = 249608$ cells with $h_{max} = 0.0051$ (denoted by “coarse”) and $N = 953688$ cells with $h_{max} = 0.0027$ (denoted by “fine”), respectively. In Fig.

3.10, we present the results of the GDF scheme on the coarse mesh at $T = 0.295$, all the quantities are resolved well. Moreover, we compare the Mach number at central area computed by the three schemes. In Fig. 3.11, we present the results of Mach number at central area on both coarse mesh and fine mesh. For the Base scheme, significant Mach number distortions are observed, while the results from the LDF and GDF schemes are considerably improved. However, in the vicinity of $(0.4, 0.45)$, it seems the Mach number computed using the LDF formulation still exhibits minor distortions.

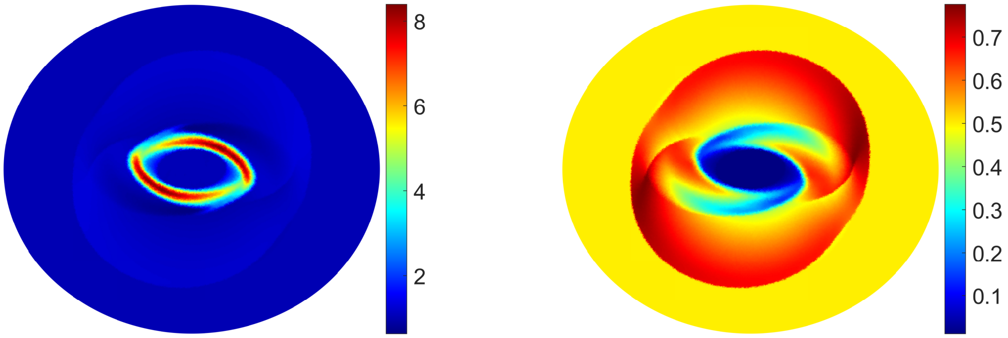

(a) Density.

(b) Pressure.

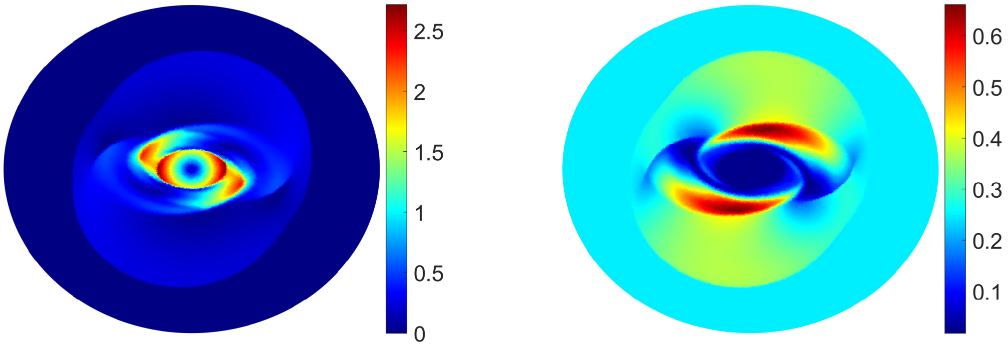

(c) Mach number $\|\mathbf{u}\|/c$.

(d) Magnetic pressure $0.5\|\mathbf{B}\|^2$.

Figure 3.10. Example 3.4: Rotor. The numerical solution on $N = 246908$ meshes at $T = 0.295$.

To further study this phenomenon, in Fig. 3.12 we compare the 1D cuts of Mach number along $x = 0.413$ and $x = 0.545$ for different schemes with mesh refinement. The reference solution (denoted by “Ref”) is computed by the LDF DG in [24] scheme on 800×800 rectangular meshes, which has been verified to be a reliable result. For the Base scheme, the solution exhibits non-physical behavior in both cross-sections. For LDF scheme, at $x = 0.545$, the scheme captures the structures well. But at $x = 0.413$, it can be seen that the result of LDF scheme deviates from the reference solution near $y = 0.45$. Moreover, this non-physical structure does not diminish with mesh refinement.

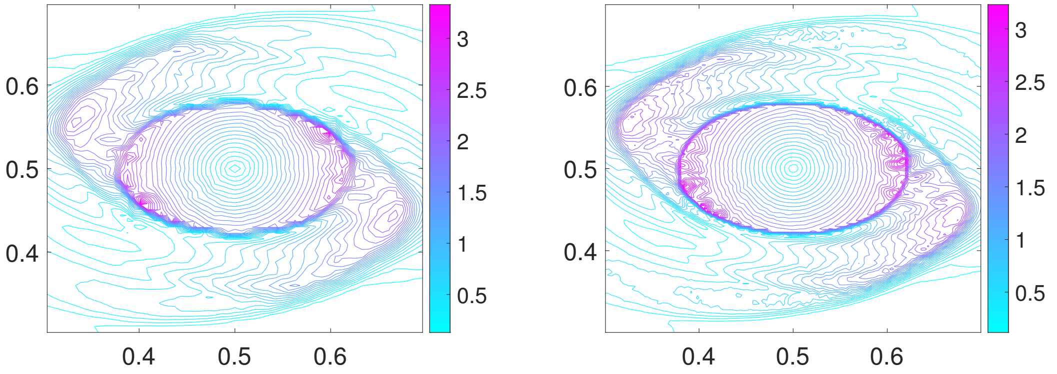

(a) Base, $N = 246908$.

(b) Base, $N = 953688$.

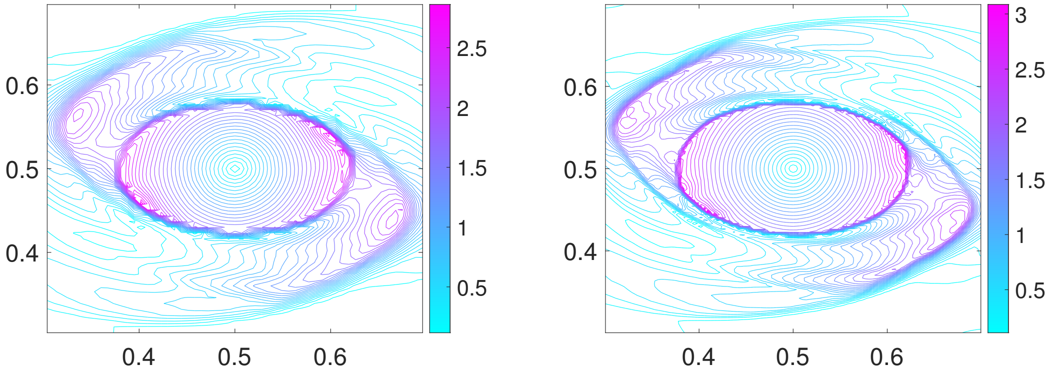

(c) LDF, $N = 246908$.

(d) LDF, $N = 953688$.

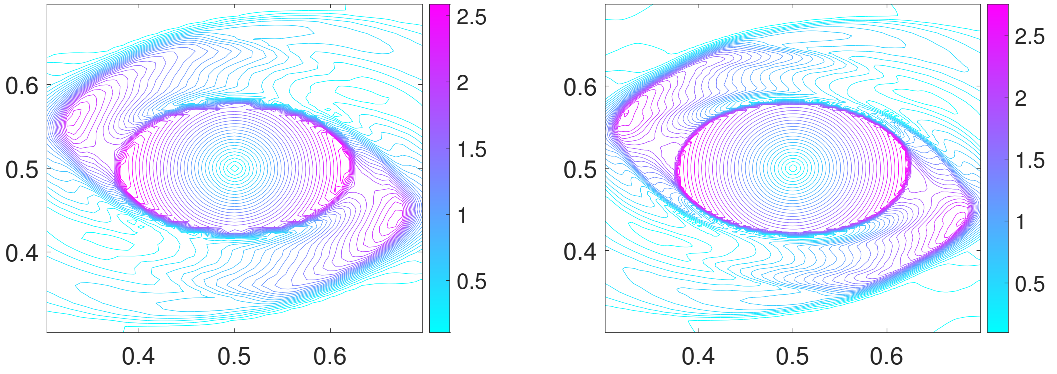

(e) GDF, $N = 246908$.

(f) GDF, $N = 953688$.

Figure 3.11. Example 3.4: Rotor. Mach number at central area with different schemes at $T = 0.295$. 30 contour lines are used.

Meanwhile, the GDF scheme resolves the Mach number well on both cross-sections, and demonstrates good convergence properties. This indicates that GDF scheme is the most stable among these three schemes for this example.

Remark 3.1. *We also test the standard setup of rotor problem on* $\Omega = [0,1] \times [0,1]$ *with a uniform triangular mesh as shown in Fig. 3.5. An interesting result is that for uniform meshes, the LDF scheme does not exhibit the distortion shown in Fig. 3.11 and Fig. 3.12, but instead converges well to the reference solution as in the rectangular case [24]. Based on this, we guess that the issue arises caused by the LDF scheme does not fully satisfy the divergence-free constraint, resulting in slight non-physical behavior when applied to complex meshes.*

Example 3.5. ***(Rotated shock tube.)***

Here, we investigate a 2D Riemann problem [37] created by rotating a one-dimensional shock tube at an angle $\alpha = \pi/4$. It is worth noting that the divergence-free property is crucial for maintaining the constancy of the parallel component $B_{||} := B_x \cos\alpha + B_y \sin\alpha$.

We will use $M_1 \times N_1 \times 2$ uniform meshes for this example, and the computational domain is defined as a rectangle $\Omega = [0,1] \times [0, N_1/M_1]$. In particular, we take $N_1 = 1$. A sample mesh is shown in Fig. 3.13. The Dirichlet boundary conditions are applied to the left and right boundaries according to the initial condition, and the top and bottom boundaries are imposed with the shifted periodic type according to the translational symmetry, as detailed in [37]. The initial data is

$$(\rho, u_x, u_y, u_z, B_x, B_y, B_z, p) = \begin{cases} \left(1, \frac{10}{\sqrt{2}}, \frac{10}{\sqrt{2}}, 0, 0, \frac{5\sqrt{2}}{\sqrt{4\pi}}, 0, 20\right), & x + y < 0.5, \\ \left(1, \frac{-10}{\sqrt{2}}, \frac{-10}{\sqrt{2}}, 0, 0, \frac{5\sqrt{2}}{\sqrt{4\pi}}, 0, 1\right), & x + y \geq 0.5. \end{cases}$$

We run this problem on $N = 512 \times 1 \times 2 = 1024$ uniform meshes. The results at $T = 0.08/\sqrt{2}$ are shown in Fig. 3.14, where the reference solution is computed by a classical third-order 1D DG scheme using TVB limiter with $M = 1$ on 10,000 cells for the non-rotated version, which can be treated as a 1D problem. Moreover, in Fig. 3.15, we plot the evolution of divergence norm and the 1D cut of divergence along x-direction at the final time. It can be seen that the $B_{||}$ component obtained by GDF scheme is the closest to constant, the LDF scheme is second, while the Base scheme exhibits the highest error. This corresponds to the same order in which they satisfy the divergence-free constraint: the GDF scheme fully satisfies the divergence-free property, the LDF scheme partially satisfies it, while the Base scheme does not satisfy the divergence-free property in any sense. Moreover, for $u_\perp$ and $B_\perp$ components, the Base scheme and LDF scheme show minor oscillations, but the oscillation of LDF scheme is smaller than Base scheme. Meanwhile, the GDF scheme gives the most stable result. As discussed in [24], it seems that the divergence-free treatments have some "smoothing" effect, which could enhance the stability of the scheme.

Example 3.6. ***(Cloud shock interaction.)***

Finally, we test the cloud shock interaction problem [35]. This test case examines a strong rightward-moving MHD shock passing a stationary bubble. The interaction

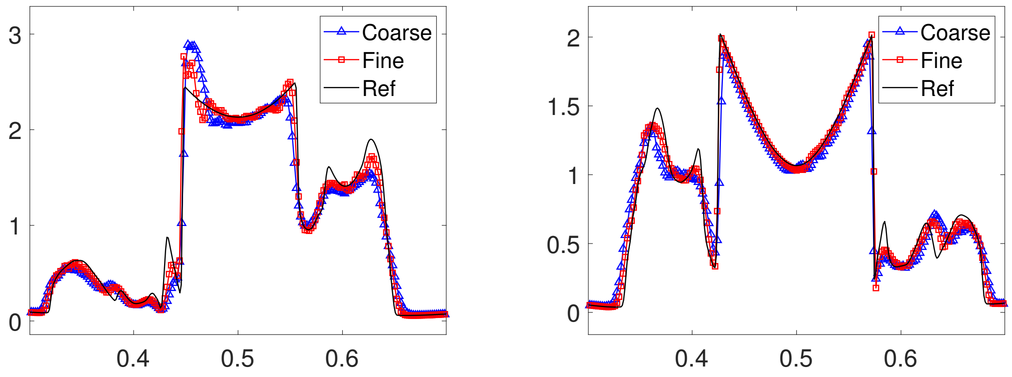

(a) Base, $x = 0.413$.

(b) Base, $x = 0.545$.

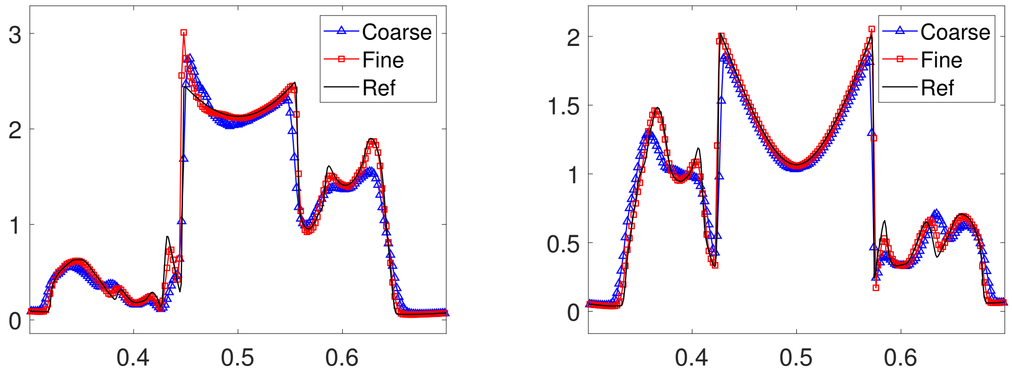

(c) LDF, $x = 0.413$.

(d) LDF, $x = 0.545$.

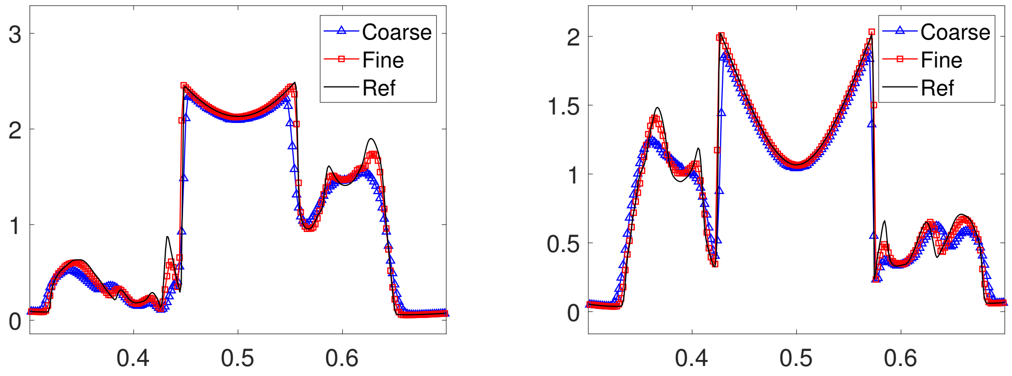

(e) GDF, $x = 0.413$.

(f) GDF, $x = 0.545$.

Figure 3.12. Example 3.4: Rotor. The 1D cuts of Mach number with mesh refinement.

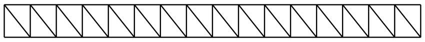

Figure 3.13. Example 3.5: Rotated shock tube. A sample mesh.

between the shock and bubble generates highly complex flow structures throughout the computational domain. These intricate formations surrounding the bubble are particularly vulnerable to numerical dissipation effects. Therefore, numerical schemes with lower dissipation offer significant advantages in capturing these structures.

The computational domain is $\Omega = [0,1] \times [0,1]$. Inflow boundary condition is applied at the left, and the remaining boundary conditions are outflow. The mesh type is same to Fig. 3.3. The initial condition consists of a shock initialized at $x = 0.05$, and a circular cloud of density 10 and radius 0.15 centered at $(0.25, 0.5)$:

$$(\rho, \mathbf{u}, \mathbf{B}, p) = \begin{cases} (3.86859, 11.2536, 0, 0, 0, 2.1826182, -2.1826182, 167.345) & \text{in } \Omega_1, \\ (10, 0, 0, 0, 0, 0, 0.56418598, 0.56418598, 1) & \text{in } \Omega_2, \\ (1, 0, 0, 0, 0, 0, 0.56418598, 0.56418598, 1) & \text{in } \Omega_3, \end{cases}$$

where

$$\begin{aligned} \Omega_1 &= \{(x,y) : x < 0.05\}, \\ \Omega_2 &= \left\{(x,y) : x \geq 0.05, \sqrt{(x-0.25)^2 + (y-0.5)^2} < 0.15\right\}, \\ \Omega_3 &= \left\{(x,y) : x \geq 0.05, \sqrt{(x-0.25)^2 + (y-0.5)^2} \geq 0.15\right\}. \end{aligned}$$

We simulate this problem until $T = 0.06$ on $N = 604640$ meshes with $h_{max} = 0.0039$. The results are presented in Fig. 3.16. Our results demonstrate that the GDF scheme effectively captures shocks and other intricate flow features with high fidelity. The computational solution shows strong agreement with previously published findings, including those presented by [10, 40, 9, 27].

4 Concluding remarks

In this paper, we propose a general globally divergence-free DG framework for solving the compressible ideal MHD equations on unstructured meshes. We improve the numerical flux selection in the updating scheme of normal magnetic components for better stability, which provides a robust framework for handling complex MHD problems. Moreover, by carefully utilizing the geometry of cell, we construct the cell-independent least-squares formulation, which allows for direct implementation through matrix mul-

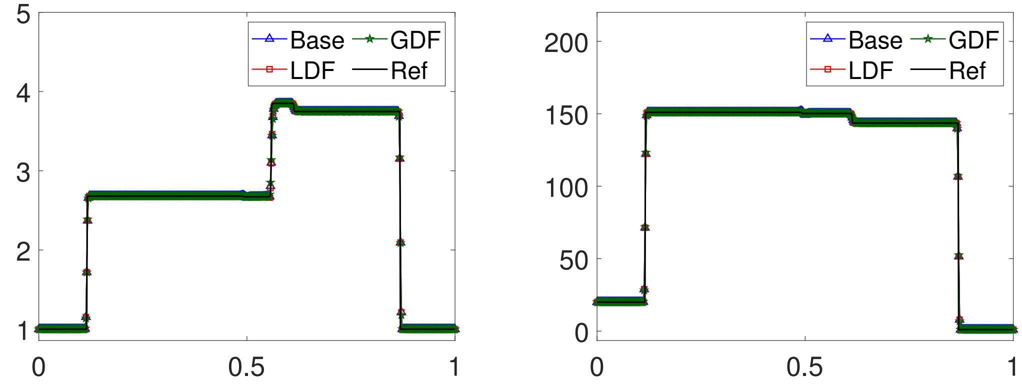

(a) ρ. (b) p.

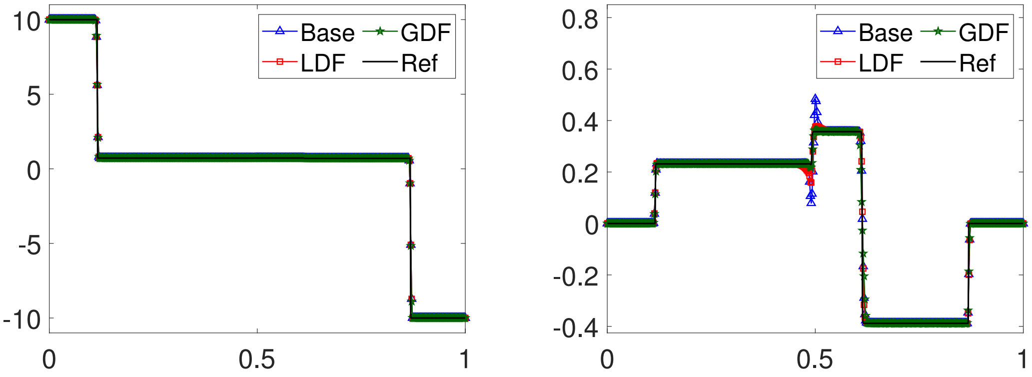

(c) $u_{||} = (u_x + u_y)/\sqrt{2}$. (d) $u_{\perp} = (-u_x + u_y)/\sqrt{2}$.

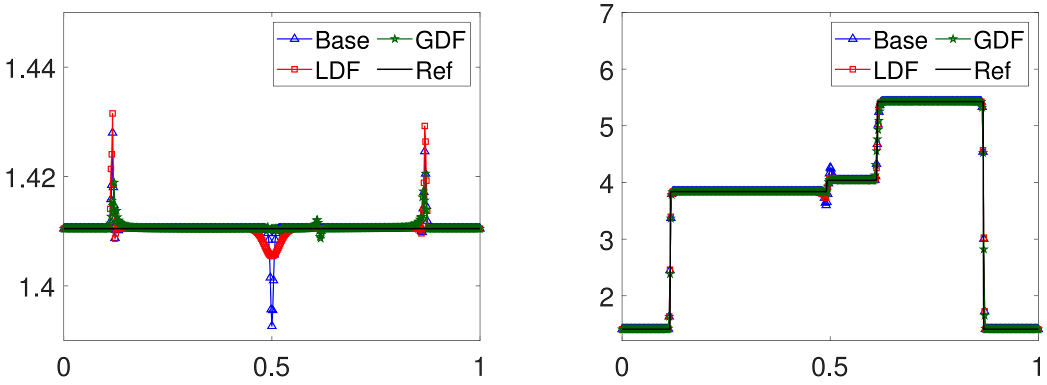

(e) $B_{||} = (B_x + B_y)/\sqrt{2}$. (f) $B_{\perp} = (-B_x + B_y)/\sqrt{2}$.

Figure 3.14. Example 3.5: Rotated shock tube. The numerical solution along $y = 0$ at $T = 0.08/\sqrt{2}$ on $N = 1024$ meshes.

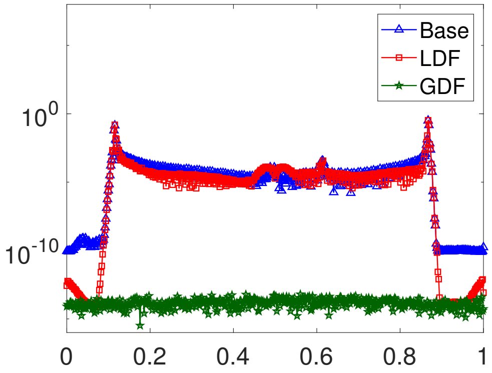

Figure 3.15. Example 3.5: Rotated shock tube. The 1D cut of divergence with different schemes at $T = 0.08/\sqrt{2}$.

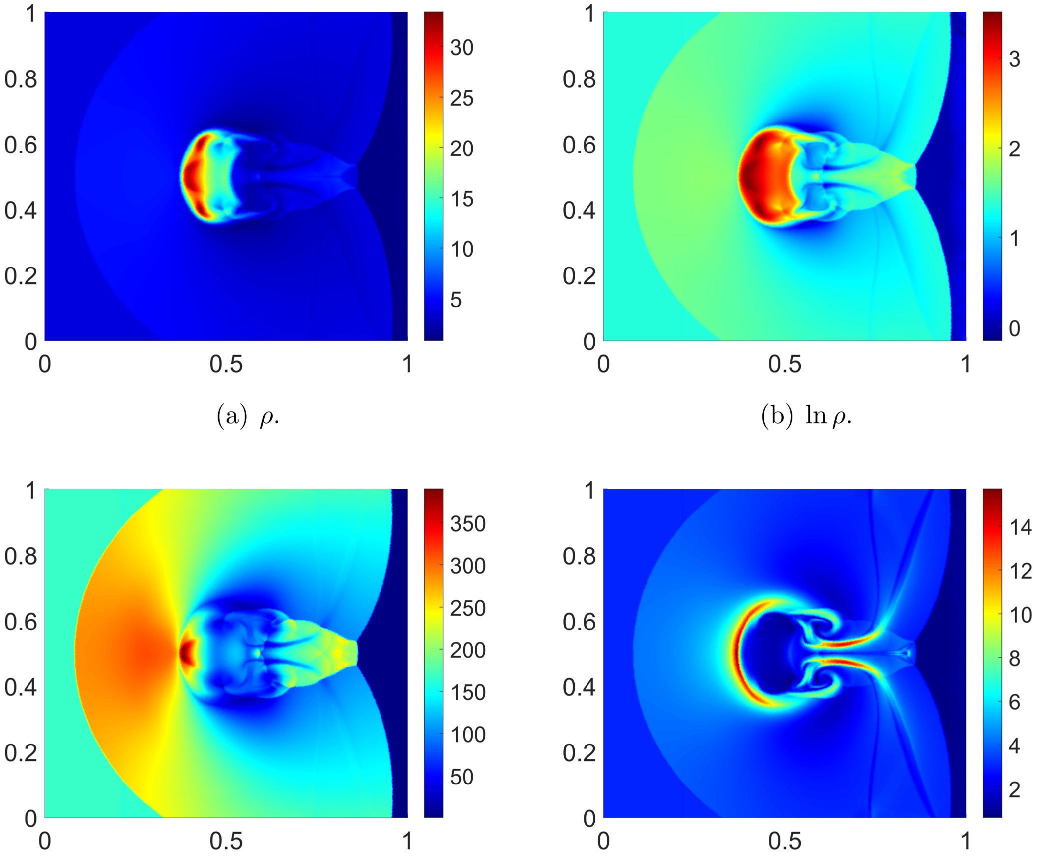

(a) ρ.

(b) $\ln \rho$.

(c) p.

(d) $\|\mathbf{B}\|$.

Figure 3.16. Example 3.6: Cloud shock interaction. The numerical solution at $T = 0.06$ on $N = 604640$ meshes.

tiplication rather than solving linear systems repeatedly, making it particularly advantageous for non-uniform or moving meshes.

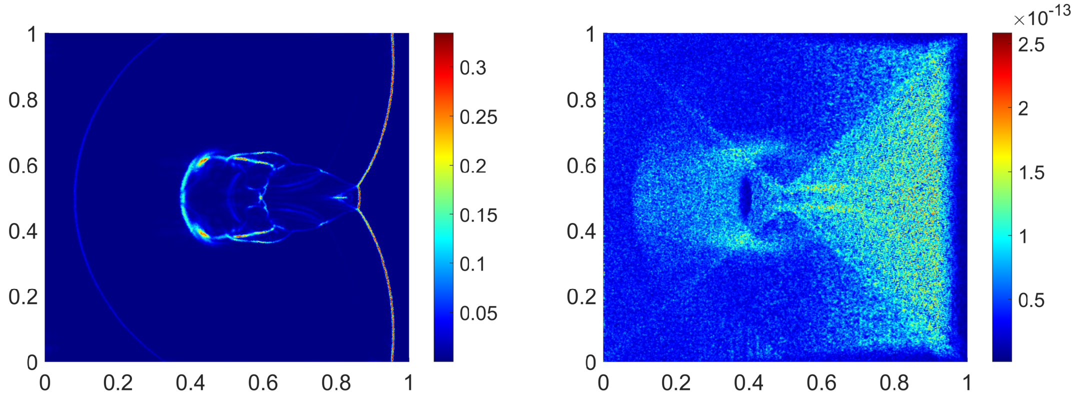

(a) LDF.

(b) GDF.

Figure 3.17. Example 3.6: Cloud shock interaction. The divergence of different schemes at $T = 0.06$.

Extensive numerical experiments conducted demonstrate that our proposed method not only achieves the designed order of accuracy for smooth problems, but also exhibits superior stability for problems involving strong discontinuities. Comparison between the base DG, locally divergence-free DG, and our globally divergence-free DG methods clearly illustrates that maintaining the divergence-free constraint at the global level is crucial for long-time simulations and complex geometries.

Future work may include combining this framework with other structure-preserving methods, such as the entropy stable method or the positivity-preserving method. Additionally, investigating the application of our method to more complex physical models such as resistive MHD or Hall MHD could be considered.

Ethics declarations

Conflict of interest

The authors declare that they have no conflict of interest.

Data Availability

Data sets generated during the current study are available from the corresponding author on reasonable request.

References

[1] D. S. Balsara. Second-order-accurate schemes for magnetohydrodynamics with divergence-free reconstruction. *The Astrophysical Journal Supplement Series*, 151(1):149, 2004.

[2] D. S. Balsara. Divergence-free reconstruction of magnetic fields and WENO schemes for magnetohydrodynamics. *Journal of Computational Physics*, 228(14):5040–5056, 2009.

[3] D. S. Balsara and M. Dumbser. Divergence-free MHD on unstructured meshes using high order finite volume schemes based on multidimensional Riemann solvers. *Journal of Computational Physics*, 299:687–715, 2015.

[4] D. S. Balsara and J. Kim. A comparison between divergence-cleaning and staggered-mesh formulations for numerical magnetohydrodynamics. *The Astrophysical Journal*, 602(2):1079, 2004.

[5] D. S. Balsara, R. Kumar, and P. Chandrashekar. Globally divergence-free DG scheme for ideal compressible MHD. *Communications in Applied Mathematics and Computational Science*, 16(1):59–98, 2021.

[6] D. S. Balsara and D. S. Spicer. A staggered mesh algorithm using high order Godunov fluxes to ensure solenoidal magnetic fields in magnetohydrodynamic simulations. *Journal of Computational Physics*, 149(2):270–292, 1999.

[7] P. Chandrashekar and R. Kumar. Constraint preserving discontinuous Galerkin method for ideal compressible MHD on 2-D Cartesian grids. *Journal of Scientific Computing*, 84(2):39, 2020.

[8] K. Chen and C. Liang. An Arbitrarily High-order Spectral Difference Method with Divergence Cleaning (SDDC) for Compressible Magnetohydrodynamic Simulations on Unstructured Grids. *The Astrophysical Journal*, 932(1):16, 2022.

[9] A. J. Christlieb, X. Feng, Y. Jiang, and Q. Tang. A high-order finite difference WENO scheme for ideal magnetohydrodynamics on curvilinear meshes. *SIAM Journal on Scientific Computing*, 40(4):A2631–A2666, 2018.

[10] A. J. Christlieb, J. A. Rossmanith, and Q. Tang. Finite difference weighted essentially non-oscillatory schemes with constrained transport for ideal magnetohydrodynamics. *Journal of Computational Physics*, 268:302–325, 2014.

[11] B. Cockburn, S. Hou, and C.-W. Shu. The Runge-Kutta local projection discontinuous Galerkin finite element method for conservation laws. IV. The multidimensional case. *Mathematics of Computation*, 54(190):545–581, 1990.

[12] B. Cockburn, F. Li, and C.-W. Shu. Locally divergence-free discontinuous Galerkin methods for the Maxwell equations. *Journal of Computational Physics*, 194(2):588–610, 2004.

[13] B. Cockburn, S.-Y. Lin, and C.-W. Shu. TVB Runge-Kutta local projection discontinuous Galerkin finite element method for conservation laws III: one-dimensional systems. *Journal of Computational Physics*, 84(1):90–113, 1989.

[14] B. Cockburn and C.-W. Shu. TVB Runge-Kutta local projection discontinuous Galerkin finite element method for conservation laws. II. General framework. *Mathematics of Computation*, 52(186):411–435, 1989.

[15] B. Cockburn and C.-W. Shu. The Runge-Kutta local projection-discontinuous-Galerkin finite element method for scalar conservation laws. *ESAIM: Mathematical Modelling and Numerical Analysis*, 25(3):337–361, 1991.

[16] B. Cockburn and C.-W. Shu. The Runge–Kutta discontinuous Galerkin method for conservation laws V: multidimensional systems. *Journal of Computational Physics*, 141(2):199–224, 1998.

[17] A. Dedner, F. Kemm, D. Kröner, C.-D. Munz, T. Schnitzer, and M. Wesenberg. Hyperbolic divergence cleaning for the MHD equations. *Journal of Computational Physics*, 175(2):645–673, 2002.

[18] C. R. Evans and J. F. Hawley. Simulation of magnetohydrodynamic flows-A constrained transport method. *The Astrophysical Journal*, 332:659–677, 1988.

[19] P. Fu, F. Li, and Y. Xu. Globally divergence-free discontinuous Galerkin methods for ideal magnetohydrodynamic equations. *Journal of Scientific Computing*, 77:1621–1659, 2018.

[20] T. A. Gardiner and J. M. Stone. An unsplit Godunov method for ideal MHD via constrained transport. *Journal of Computational Physics*, 205(2):509–539, 2005.

[21] K. Hu, Y. Ma, and J. Xu. Stable finite element methods preserving $\nabla \cdot \mathbf{B} = 0$ exactly for MHD models. *Numerische Mathematik*, 135(2):371–396, 2017.

[22] D. I. Ketcheson. Highly efficient strong stability-preserving Runge–Kutta methods with low-storage implementations. *SIAM Journal on Scientific Computing*, 30(4):2113–2136, 2008.

[23] C. Klingenberg, F. Pörner, and Y. Xia. An efficient implementation of the divergence free constraint in a discontinuous Galerkin method for magnetohydrodynamics on unstructured meshes. *Communications in Computational Physics*, 21(2):423–442, 2017.

[24] F. Li and C.-W. Shu. Locally divergence-free discontinuous Galerkin methods for MHD equations. *Journal of Scientific Computing*, 22(1):413–442, 2005.

[25] F. Li and L. Xu. Arbitrary order exactly divergence-free central discontinuous Galerkin methods for ideal MHD equations. *Journal of Computational Physics*, 231(6):2655–2675, 2012.

[26] F. Li, L. Xu, and S. Yakovlev. Central discontinuous Galerkin methods for ideal MHD equations with the exactly divergence-free magnetic field. *Journal of Computational Physics*, 230(12):4828–4847, 2011.

[27] Y. Liu, W. Guo, Y. Jiang, and M. Zhang. A globally divergence-free entropy stable nodal DG method for conservative ideal MHD equations. *arXiv preprint arXiv:2501.06815*, 2025.

[28] Y. Liu, Y. Jiang, and M. Zhang. Globally divergence-free spectral-DG methods for MHD equations on cylindrical coordinates. *Beijing Journal of Pure and Applied Mathematics*, 2(1):285–324, 2025.

[29] Y. Liu, C.-W. Shu, and M. Zhang. Entropy stable high order discontinuous Galerkin methods for ideal compressible MHD on structured meshes. *Journal of Computational Physics*, 354:163–178, 2018.

[30] X.-H. Luo, B.-W. Li, J.-K. Zhang, and Z.-M. Hu. Simulation of thermal radiation effects on MHD free convection in a square cavity using the Chebyshev collocation spectral method. *Numerical Heat Transfer, Part A: Applications*, 66(7):792–815, 2014.

[31] T. Minoshima, T. Miyoshi, and Y. Matsumoto. A high-order weighted finite difference scheme with a multistate approximate Riemann solver for divergence-free magnetohydrodynamic simulations. *The Astrophysical Journal Supplement Series*, 242(2):14, 2019.

[32] S. A. Orszag and C.-M. Tang. Small-scale structure of two-dimensional magnetohydrodynamic turbulence. *Journal of Fluid Mechanics*, 90(1):129–143, 1979.

[33] K. G. Powell, P. L. Roe, T. J. Linde, T. I. Gombosi, and D. L. De Zeeuw. A solution-adaptive upwind scheme for ideal magnetohydrodynamics. *Journal of Computational Physics*, 154(2):284–309, 1999.

[34] W. H. Reed and T. R. Hill. Triangular mesh methods for the neutron transport equation. Technical report, Los Alamos Scientific Lab., N. Mex.(USA), 1973.

[35] J. A. Rossmanith. An unstaggered, high-resolution constrained transport method for magnetohydrodynamic flows. *SIAM Journal on Scientific Computing*, 28(5):1766–1797, 2006.

[36] C.-W. Shu. Essentially non-oscillatory and weighted essentially non-oscillatory schemes. *Acta Numerica*, 29:701–762, 2020.

[37] G. Tóth. The $\nabla \cdot \mathbf{B} = 0$ constraint in shock-capturing magnetohydrodynamics codes. *Journal of Computational Physics*, 161(2):605–652, 2000.

[38] M. H. Veiga, D. A. Velasco-Romero, Q. Wenger, and R. Teyssier. An arbitrary high-order spectral difference method for the induction equation. *Journal of Computational Physics*, 438:110327, 2021.

[39] L. Wei, L. Zhou, and Y. Xia. The jump filter in the discontinuous Galerkin method for hyperbolic conservation laws. *Journal of Computational Physics*, page 113498, 2024.

[40] K. Wu. Positivity-preserving analysis of numerical schemes for ideal magnetohydrodynamics. *SIAM Journal on Numerical Analysis*, 56(4):2124–2147, 2018.

[41] Z. Xu, D. S. Balsara, and H. Du. Divergence-free WENO reconstruction-based finite volume scheme for solving ideal MHD equations on triangular meshes. *Communications in Computational Physics*, 19(4):841–880, 2016.

[42] Z. Xu and Y. Liu. New central and central discontinuous Galerkin schemes on overlapping cells of unstructured grids for solving ideal magnetohydrodynamic equations with globally divergence-free magnetic field. *Journal of Computational Physics*, 327:203–224, 2016.

[43] Y. Yu, Y. Jiang, and M. Zhang. Free-stream preserving finite difference schemes for ideal magnetohydrodynamics on curvilinear meshes. *Journal of Scientific Computing*, 82(1):1–26, 2020.